



Full Text View

[Volume 30, Issue 1 \(January 2000\)](#)

Journal of Physical Oceanography

 Article: pp. 3–14 | [Abstract](#) | [PDF \(228K\)](#)

Interannual Geostrophic Current Anomalies in the Near-Equatorial Western Pacific

T. M. Shaun Johnston and Mark A. Merrifield
Department of Oceanography, School of Ocean and Earth Science and Technology, University of Hawaii at Manoa, Honolulu, Hawaii

(Manuscript received May 8, 1998, in final form October 19, 1998)

DOI: 10.1175/1520-0485(2000)030<0003:IGCAIT>2.0.CO;2

ABSTRACT

A network of island tide gauges is used to estimate interannual geostrophic current anomalies (GCAs) in the western Pacific from 1975 to 1997. The focus of this study is the zonal component of the current averaged between 160°E and 180° and 2° to 7° north and south of the equator in the mean flow regions associated with the North Equatorial Countercurrent (NECC) and the South Equatorial Current (SEC), respectively. The tide gauge GCA estimates agree closely with similarly derived currents from TOPEX/Poseidon sea level anomalies. The GCAs in the western Pacific relate to a basin-scale adjustment associated with the El Niño–Southern Oscillation, characterized here using empirical orthogonal functions of tide gauge and supporting sea surface temperature and heat storage data. The dominant EOF mode describes the mature phase of ENSO events and correlates (0.8) with the GCA south of the equator. The second mode describes transitions to and from ENSO events and correlates (0.9) with the GCA north of the equator. The typical scenario then is for the NECC to intensify about 6 months prior to the peak of an El Niño, to remain near mean conditions during the peak stage of El Niño, and to later weaken about 6 months following the peak. In contrast, the SEC generally weakens throughout an El Niño displaying eastward anomalies. This equatorial asymmetry in the GCAs is consistent with a similar asymmetry in the wind field over the western Pacific. The phase differences between the NECC and SEC are less apparent during La Niña events. The GCA results provide further evidence that transitional phases of ENSO are more active north than south of the equator in the warm pool region.

Table of Contents:

- [Introduction](#)
- [Data](#)
- [Geostrophic current anomalies](#)
- [Description of the interannual](#)
- [Wind forcing and the](#)
- [Summary and discussion](#)
- [REFERENCES](#)
- [FIGURES](#)

Options:

- [Create Reference](#)
- [Email this Article](#)
- [Add to MyArchive](#)
- [Search AMS Glossary](#)

Search CrossRef for:

- [Articles Citing This Article](#)


Search Google Scholar for:

- [T. M. Shaun Johnston](#)
- [Mark A. Merrifield](#)

The variability of zonal flow in the equatorial Pacific and its effect on the western Pacific warm pool was examined by [Wyrcki \(1979\)](#), who related trade wind relaxations during El Niño with an eastward transport of mass and heat out of the warm pool region. In particular, analysis of the 1976–77 El Niño based on tide gauge data showed decreased transport in the westward South Equatorial Current (SEC) and a coincident intensification of the eastward North Equatorial Countercurrent (NECC) that contributed to lower sea level in the western Pacific ([Wyrcki 1979](#)). [Wyrcki \(1985\)](#) later proposed that the El Niño–Southern Oscillation (ENSO) is governed by a buildup and release of heat and mass in the warm pool with zonal transport being the primary agent.

Zonal transport has also been shown to influence tropical Pacific sea surface temperature, a highly sensitive variable for coupled ocean–atmosphere models. [Picaut and Delcroix \(1995\)](#) find that zonal advection and wave dynamics both contribute to the generation and migration of El Niño–related SST anomalies with zonal advection playing the major role in the central and western Pacific, and wave-induced upwelling and downwelling in the eastern Pacific. Water parcels from the western Pacific warm pool traveled to about 140°–150°W during the 1986–87 El Niño ([Picaut and Delcroix 1995](#); [Delcroix and Picaut 1998](#)). During the 1991–93 El Niño, [Kessler and McPhaden \(1995\)](#) estimate zonal advection scales to be 500–1000 km. [Kessler and McPhaden \(1995\)](#) also describe how zonal advection, meridional advection, and upwelling were important in determining SST variations on different timescales and at different phases of the 1991–92 warm event. [Frankignoul et al. \(1996\)](#) summarize various observational and model analyses related to this issue.

In short, an accurate specification of the variability of zonal transport is an important consideration toward understanding and modeling equatorial dynamics. The observational record on zonal currents, particularly just off the equator, is provided primarily by geostrophic estimates using expendable bathythermograph (XBT) and tide gauge data, moored buoys in the Tropical Atmosphere–Ocean (TAO) array, and surface drifters. Estimates of zonal current variations based on tide gauge differences show the NECC at maximum eastward flow when the SEC is at a minimum in westward flow, or that the two zonal current systems tend to fluctuate in phase ([Wyrcki 1974a, b; 1979](#)). This was later confirmed using geostrophic transport from XBT data in the central Pacific (25°N to 20°S, 150°W to 180°) from 1970 to 1987 ([Kessler and Taft 1987](#); [Taft and Kessler 1991](#)). During the 1991–92 El Niño near 140°W, [Kessler and McPhaden \(1995\)](#) report near-zero net surface flow between 7°S and 4°N, suggesting that the relationship may not hold for all El Niño events. In the western Pacific, [Meyers and Donguy \(1984\)](#) analyzed geostrophic zonal flow for the 1982–83 El Niño using XBT data along the Japan–New Caledonia shipping line. They found a strengthening of the NECC during the early phase of the event (August 1982) followed by a weakening to near zero flow 10 months later. During the same period, the SEC exhibited a southward shift causing a weakening of the flow near the equator.


Near-equatorial currents have been measured directly using drogued surface drifters and TAO current meters. [Frankignoul et al. \(1996\)](#) used these datasets to produce current anomaly fields from May 1988 to August 1992 that show anomalous westward flow over a broad region of the equatorial Pacific prior to and after the peak of the 1991–92 El Niño and anomalous eastward flow during the peak of the event. Although the zonal current anomalies tend to span the basin, currents north and south of the equator can differ significantly at any given time, particularly in the western Pacific (see their [Fig. 7](#) ). These near-surface observations reflect both frictionally wind-driven as well as geostrophic contributions.

With regard to the dynamics of zonal current fluctuations near the equator, it is well established that wind-forced Rossby and Kelvin waves play a major role. Wind-forced upwelling Rossby waves emanating from the eastern boundary are linked to a transition from El Niño to La Niña conditions and from eastward to westward current anomalies ([Delcroix et al. 1994](#); [Picaut and Delcroix 1995](#)). In particular, the first baroclinic Kelvin and first symmetric Rossby modes have been shown to play the largest role in the zonal advection of the western Pacific warm pool during the 1986–87 El Niño and the 1988–89 La Niña ([Delcroix et al. 1994](#); [Picaut and Delcroix 1995](#)). The influence of equatorial wave modes extend to within 1°–2° of the equator, or an equatorial Rossby radius. At higher latitudes, long Rossby waves have been observed at interannual timescales propagating westward in the North Pacific ([Graham and White 1991](#); [Tourre and White 1995](#); [Zhang and Levitus 1996](#)) having been generated by wind stress curl anomalies associated with ENSO ([Kessler 1990, 1991](#)). [Kessler \(1991\)](#) distinguishes between quickly propagating near-equatorial waves within 8° of the equator that can contribute to wave reflections at the western boundary and much slower extra-equatorial waves farther north, which apparently do not directly affect the equatorial waveguide.

A network of island tide gauges has been in place in the western Pacific since the early 1970s, providing one of the longest continuous oceanographic records in the region. Based on relative sea-level differences obtained from these gauges, [Wyrcki \(1974a\)](#) developed GCA indices for the major equatorial current systems. We revisit this analysis from a slightly different approach. Here we seek to determine zonal GCAs in the western Pacific using estimates of sea surface gradients obtained from the tide gauge network. Because of the position of the gauges, the focus is on off-equatorial zonal currents from 160°E to 180°. Our intent is to compare the interannual variations of currents north and south of the equator in the western Pacific and to relate these variations to the dominant interannual signal in the region, namely ENSO. Our main findings are that the current variations in the western Pacific are not in phase as has been reported in the central Pacific. Instead, the current variations north and south of the equator relate to different phasings of ENSO. Specifically, northern current anomalies tend to peak during transitions in ENSO, while the southern anomalies are in phase with ENSO.

This analysis is presented as follows: The various datasets used in this study are described in [section 2](#). In [section 3](#), we present the GCA estimates from the tide gauges and validate these estimates using GCAs derived from TOPEX/Poseidon (T/P) altimeter data. To place these observations in the context of ENSO variations, we use EOFs based on tide gauge sea level as well as supporting SST and heat storage data to show how zonal currents relate to the dominant interannual variability over the equatorial Pacific in [section 4](#). The two dominant EOF modes describe variability in phase with the mature stage of ENSO (mode 1), or equivalently the Southern Oscillation index (SOI), and variability in quadrature with the SOI, which emphasizes ENSO transition phases (mode 2). Similar variability has been identified in a variety of datasets ([Latif and Flügel 1991](#); [Ji et al. 1995](#); [Zhang and Levitus 1996, 1997](#)). Together the two modes describe phase propagation associated with ENSO ([Tourre and White 1995](#); [Zhang and Levitus 1996](#)). These combined EOF modes are then regressed onto the zonal wind stress (ZWS) ([section 5](#)) to emphasize the dominant wind patterns that correlate with these modes and the estimated currents. In addition, we illustrate the relationship between GCAs and winds using a composite wind anomaly from three El Niño events ([section 5](#)). In [section 6](#), we summarize the main results of this study and discuss the asymmetric GCA variability in the context of wind forcing and wave propagation. We end by considering some implications of these GCAs for the western Pacific warm pool and ENSO events.

2. Data

This investigation uses monthly mean sea level data from 43 island and coastal tide gauges in the tropical Pacific obtained from the University of Hawaii Sea Level Center. Records extend over most of the time period from January 1975 to November 1997 ([Kilonsky and Caldwell 1991](#)). Spatial coverage is good in the western Pacific and poor in the eastern Pacific ([Fig. 1](#) ).

The NOAA Laboratory for Satellite Altimetry produces monthly T/P sea level anomalies on a 1° latitude by 4° longitude grid beginning in September 1992. The anomalies are formed by removing the 3-yr mean from 1993 to 1995 and the annual and semiannual harmonics. The root-mean-square difference between tide gauges in the tropical Pacific and T/P is about 2 cm over spatial scales of several hundred kilometers ([Cheney et al. 1994](#)). Our analysis uses anomalies within 30° of the equator from 124°E to 70°W .

Sea surface temperature (SST) anomalies from 1982 to 1997 are formed from the Reynolds SST monthly means in the tropical Pacific ([Reynolds and Marisco 1993](#)). We use a subset of the data on a 2° latitude by 5° longitude grid from 34.5°N to 33.5°S , 120.5°E to 74.5°W . The SST data, which are a combination of in situ and satellite measurements, provide spatial coverage in areas where the tide gauge network is sparse.

The Joint Environmental Data Analysis Center provides heat storage anomalies in the upper 400 m (HS400) of the ocean in a 2° latitude by 5° longitude grid ([Tourre and White 1995](#)). Most data are gathered by XBT and are available from 1955 to 1994. Spatial coverage emphasizes established shipping lanes, so little data are available in the eastern South Pacific. Our analysis uses data from 36°N to 36°S , 120°E to 70°W .

Zonal and meridional wind pseudostress for the tropical Pacific are available from The Florida State University's (FSU) Center for Ocean–Atmospheric Prediction Studies. The FSU wind pseudostress product is compiled from surface marine reports from 1961 to the present and is gridded in 2° by 2° squares between 124°E and 70°W within 29° of the equator ([Goldenberg and O'Brien 1981](#)). The pseudostress is the wind vector scaled by the wind magnitude, which can be multiplied by the air density and a drag coefficient to yield the wind stress.

For the tide gauge, HS400, SST, and FSU wind datasets, anomalies are obtained by removing a linear trend, mean, and semiannual and annual harmonics from each record. The monthly anomalies are filtered using a 13-month Gaussian running mean. Data gaps shorter than or equal to 4 months in the tide gauge records are filled by linear interpolation in time. Longer gaps in tide gauge data and all gaps in HS400 are filled by spatial interpolation using continuous curvature splines in tension ([Smith and Wessel 1990](#); [Wessel and Smith 1995](#)). This interpolation method also is used to map sea level anomalies from irregularly spaced tide gauges onto a 1° latitude by 2.5° longitude grid. The surface is the solution of the equation $(1 - T)\nabla^4 H + \nabla^2 H = 0$, where T is the tension set at 0.25, ∇^2 is the Laplacian operator, and H is the sea level anomaly. This is the sea level anomaly from tide gauges that is used in the rest of this paper.

3. Geostrophic current anomalies in the western Pacific

We obtain zonal and meridional GCAs from sea level anomalies using $u = -gH_y/f$ and $v = gH_x/f$, respectively, where g is the acceleration due to gravity, f is the Coriolis parameter, H_y is the meridional sea level anomaly gradient, and H_x is the zonal gradient. We compute partial derivatives using centered differences of the gridded anomaly fields. The zonal difference is scaled by the cosine of the latitude. GCAs inferred from tide gauge data provide temporal coverage extending back to 1975, whereas T/P anomalies provide high spatial resolution across the tropical Pacific since 1992.

The tide gauge network best resolves GCAs in the area within 7° of the equator in the western Pacific near 160°E, where the tide gauge stations are most densely spaced and the sea level gradients are relatively large (Fig. 2). The northern and southern GCAs modulate the mean flow in regions generally associated with the eastward flowing NECC and westward SEC, respectively. These variations are related to ENSO events, which can be defined by large departures of the SOI from its mean value (Fig. 3c). For example, prior to the peak of the 1982–83 El Niño (July 1982, Fig. 2a), eastward GCAs occur north of the equator in the western Pacific that intensify the eastward NECC. Following the peak (July 1983, Fig. 2b) westward GCAs reduce the strength of the NECC. At both times the SEC weakens due to eastward anomalies south of the equator.

To characterize the temporal variability of the dominant zonal component of the GCAs in this region, we average the zonal anomaly from 2° to 7° north and south of the equator and between 160°E and 180° (Figs. 3a,b). To determine whether the tide gauge derived currents are representative of the actual flow, we compare the tide gauge and T/P GCAs for the overlap period. The currents are highly correlated (0.98) both north and south of the equator in the region from 160°E to 180° (Figs. 3a,b). The correlation declines for similarly averaged currents to the east of this region where the tide gauge network is sparse. The similarity of the tide gauge and altimeter derived currents suggests that tide gauges can monitor interannual variability of geostrophic currents in the western Pacific when sea level gradients are suitably averaged.

The two current systems fluctuate differently with a correlation of only 0.40 (Figs. 3a,b). In relation to ENSO warm and cold events, the GCAs north of the equator tend to intensify the NECC about 6 months prior to the peak of an El Niño or warm event (specified here by the SOI in Fig. 3c), to remain near mean conditions during the peak of the event, and to later weaken about 6 months following the peak. In contrast, the GCAs south of the equator display eastward anomalies over the duration of the El Niño, causing the SEC to weaken. Meyers and Donguy (1984) report a similar pattern for the 1982–83 event based on XBT data in the western Pacific. As noted earlier, previous studies have shown that the NECC and SEC tend to fluctuate more in phase in the central Pacific at interannual timescales (Wyrski 1977, 1979; Meyers and Donguy 1984; Kessler and Taft 1987; Taft and Kessler 1991).

During the La Niñas or cold events of 1975–76 and 1988–89, both current systems exhibit a westward anomaly that tends to weaken the NECC and strengthen the SEC (Figs. 3a,b). In contrast to the El Niño events, the two currents fluctuate more in phase with the SOI during the La Niñas. The GCA is stronger in amplitude and somewhat longer in duration in the SEC than the NECC. We emphasize that these general characteristics differ in detail for each of the various events, just as ENSO events themselves vary. For example, the SEC experiences a dip in eastward anomaly during the peak of the 1982–83 El Niño in contrast to other warm events. In general, however, the GCAs in the two averaging regions tend to fluctuate with the SOI, except for the NECC, which strengthens during the early stages of El Niño and reaches a maximum westward anomaly following the peak of the event. It is this general behavior that we examine in more detail in the following sections.

4. Description of the interannual variability

We use EOFs to examine the relationship between the GCAs in the western Pacific and basin-scale sea level, HS400, and SST variability. We will relate NECC and SEC anomalies in the western Pacific to distinctive basin-scale sea level patterns captured by the two leading EOF modes (Fig. 4). First we examine tide gauge records separately to take advantage of the long records, to update previous sea level studies (Wyrski and Wenzel 1984; Mitchum 1993), and to complement previous analyses based on HS400 data (Zhang and Levitus 1996, 1997). In the second analysis we emphasize the connection between sea level, HS400, and SST anomalies using a combined EOF based on the correlation matrix of all three variables. In addition, the HS400 and SST fields provide better coverage of the eastern Pacific than the tide gauges.

a. EOF analysis of sea level

The tide gauge EOF analysis reveals two dominant interannual modes of sea level variability in the tropical Pacific related to ENSO. The first EOF mode, accounting for 42% of the observed variability, characterizes the familiar east–west seesaw spatial pattern of warm and cold events (Fig. 4a). During warm events, anomalously high sea level occurs in the eastern Pacific and low sea level in the western Pacific. The pattern reverses during cold events. On the equator, the pivot region occurs just east of the date line. We note that contours in the eastern Pacific reflect the lack of tide gauges in this region. The first EOF temporal expansion (Fig. 4c) is highly correlated (−0.86) with the SOI, indicating that this mode is associated with the mature phase of ENSO events.

The second EOF mode, accounting for 19% of the observed variability, shows a north–south spatial pattern with a zero-crossing between 5° and 10°N (Fig. 4b). This mode describes fluctuations that precede El Niño events by up to 10 months (Fig. 4c). This behavior has been identified in previous analyses as a precursor to ENSO (Latif and Flügel 1991; Tourre and White 1995). Previous investigations using tide gauge data (Wyrski and Wenzel 1984; Latif and Flügel 1991; Mitchum 1993), HS400 (Tourre and White 1995; Zhang and Levitus 1996), and dynamical model-based ocean reanalysis (Ji et al. 1995) all describe similar first and second mode behavior. The mode 2 signal in the tide gauge data peaks in the western Pacific at 10°N and in the central Pacific at 5°S. The first and second mode each describe interannual sea level

changes of up to ± 0.3 m.

Interannual variations in the northern (NECC) and southern (SEC) GCAs are well correlated with the tide gauge EOFs (Fig. 5). The NECC anomaly (Fig. 5a) correlates with EOF mode 2 (0.90), while the SEC anomaly (Fig. 5b) correlates with mode 1 (0.76). Thus, in the western Pacific, the surface geostrophic current south of the equator fluctuates with the mature phase of El Niño, while north of the equator the geostrophic current varies more in phase with El Niño transitions. Inspection of the spatial structure in Fig. 4b indicates that mode 2 has strong meridional gradients in the Northern Hemisphere but not the Southern, consistent with the GCAs. On the other hand, mode 1 (Fig. 4a) appears more symmetric about the equator in this region. The meridional gradients in mode 2 apparently overshadow mode 1 north of the equator, particularly farther to the west. We note that for the remainder of the paper, we have used the region 140° – 160° E instead of 160° E– 180° to represent the northern GCA. The two regions have similar GCAs (note the correspondence between Figs. 3a and 5a), but the correlations between the GCAs and other parameters are slightly higher for the region farther west. This is consistent with increased mode 1 contribution in the north closer to the date line (Fig. 4a).

b. Combined EOF analysis of sea level, HS400, and SST

Even though the sea level EOFs reflect the uneven spatial sampling of the tide gauges, similar modes of variability appear in other data. To illustrate the connection between sea level, HS400, and SST anomalies, we calculate a combined EOF based on the correlation matrix of all three variables. The combined EOF temporal expansions show high correlations (0.90) with the sea level only temporal expansions, and the sea level spatial patterns are similar in both EOF analyses, suggesting that these modes are robust and not an artifact of the tide gauge sampling. Since the combined modes are obtained from a correlation matrix analysis, the EOF spatial patterns do not necessarily scale with the amplitude of the modal variability. To correct for this, we regress the first and second mode temporal expansions (Fig. 6c) onto the separate datasets using a least squares fit (Figs. 6 and 7).

The modes 1 and 2 spatial patterns for HS400 are similar to sea level and account for similar percentages of the observed variability (37% and 20%, respectively). A strong correspondence between sea level and heat storage throughout the tropical Pacific is well established (Rébert et al. 1985). Our HS400 EOFs also agree well with previous EOF analyses of heat storage (Tourre and White 1995; Zhang and Levitus 1996). The tide gauges emphasize variability in the western Pacific; however, the second HS400 EOF shows the basinwide extent of alternating zonal bands of positive and negative HS400 anomalies associated with this mode. In agreement with tide gauge results the strongest signals are located at about 10° N in the western Pacific and 5° S in the central Pacific. The two leading EOFs describe maximum interannual changes in heat storage of up to ± 2 GJ m^{-2} .

Although modal sea level, HS400, and SST have identical time dependence in this combined EOF analysis (Fig. 6c), the spatial structure of the SST modes differs from sea level and HS400. The SST mode 1 pattern (54% of the variability) shows typical ENSO behavior with a tongue of anomalously warm water extending from the west coast of South America to 160° W during El Niño events (Fig. 7a). This warm water lies within 5° of the equator and does not spread poleward along the eastern ocean boundary as extensively as sea level and HS400. The SST mode 2 pattern (9% of the variability) is associated with anomalous warming and cooling along the intertropical convergence zone (ITCZ) and South Pacific convergence zone (SPCZ) (Fig. 7b) (Tourre and White 1995). The ITCZ and SPCZ shift eastward and meet near the date line prior to the peak phase of El Niño. Cold SST anomalies are seen in the wake of the convergence zones after their eastward shift. Also, anomalously cold SST is seen in the eastern Pacific wedged between the convergence zones and the South American coast. Our first EOF mode for SST is comparable to previous work (Ji et al. 1995; Tourre and White 1995; Zhang and Levitus 1996), but explains 10%–30% more of the variability presumably due to the different meridional extent of the various analyses. Our second EOF mode is similar to that of Ji et al. (1995) and Tourre and White (1995), whereas the mode 2 of Zhang and Levitus (1996) does not capture the position of the SPCZ. We find mode 1 SST maxima displaced westward of HS400 maxima in agreement with Tourre and White (1995). Our first and second EOFs together show maximum interannual changes of $\pm 2^{\circ}$ C.

Various interpretations of the north–south asymmetry near the equator characterized by EOF mode 2 have been presented. These include interannual oscillations in the strength of the northern and southern subtropical anticyclonic gyres (Wyrtki and Wenzel 1984), ENSO-related cyclonic propagation of subsurface thermal anomalies around the North Pacific (White 1994; Tourre and White 1995; Zhang and Levitus 1996, 1997), a distinction between northern and southern ENSO events (Mitchum 1993), and sea level response to changing wind stress curl patterns (Ji et al. 1995). Zhang and Levitus (1996) demonstrate how the two leading modes together describe zonal phase propagation that is eastward along the equator and westward north of the equator in the form of long Rossby waves. This behavior was reported earlier by Tourre and White (1995). Off the equator, the westward propagation is less obvious in SST (Tourre and White 1995). The EOF modes thus describe a combination of direct wind forcing, which itself involves phase propagation and Rossby and Kelvin waves.

To illustrate the asymmetry of off-equatorial GCAs in the western Pacific, we regress the EOF mode 1 and 2 temporal expansions onto zonal currents obtained from T/P anomalies. We average T/P GCAs zonally over 20° longitude bins and

meridionally between 2° and 7°N/S. The EOF modes are scaled to unit variance for this regression. The north–south asymmetry in the GCAs is evident west of the date line (Fig. 8). North of the equator, mode 1 becomes relatively weaker in importance west of 170°E relative to the region farther east. In contrast south of the equator and west of the date line, mode 1 reaches a peak amplitude while mode 2 is relatively unimportant. In the central and eastern Pacific the two leading EOF modes are more stable in amplitude, suggesting a more symmetric current response on either side of the equator.

5. Wind forcing and the geostrophic current anomalies

ENSO variability in the ocean is strongly coupled with zonal wind stress (ZWS) anomalies in the western and central Pacific [e.g., see McPhaden et al. (1998) for a review]. In this section we examine the relationship between off-equatorial GCAs in the western Pacific and wind forcing as represented by the FSU wind pseudostress. In particular, we are interested in whether the ZWS can account for the observed asymmetry in the GCA on either side of the equator. Within about 1°–2° of the equator, equivalent to an equatorial Rossby radius, we expect the currents to respond directly to the wind stress. Farther away from the equator, however, we expect a stronger correspondence with the curl of the wind stress. Because the fluctuations in ZWS resemble those in the wind stress curl in the northern (correlation = 0.81) and southern (–0.87) averaging regions, we will continue to use the ZWS as an indicator of the wind forcing.

A comparison of the north and south GCAs with ZWS averaged over the same regions shows that the currents closely resemble the local wind forcing (Fig. 9). North of the equator, the ZWS and GCA have a maximum correlation of 0.70 with the wind leading the current by 2 months. South of the equator, the ZWS and GCA have a maximum correlation of 0.80 at zero time lag.

The regions of the ZWS field that correlate with the combined EOF modes are illustrated by regressing the temporal expansions of the EOF analysis onto the ZWS data. EOF mode 1 accounts for 19% of the ZWS variability and is associated with westerly ZWS anomalies in the central Pacific during the peak phase of El Niño (Fig. 10a). EOF mode 2, accounting for 10% of the variability, corresponds to strong westerlies that develop in the western North Pacific prior to the peak phase of El Niño (Fig. 10b). There is some indication that wind fluctuations along the SPCZ correlate with this mode in accordance with the SST modal pattern (Fig. 7b) although the relationship is not strong, perhaps due to the lack of wind observations in this region. The wind anomaly changes sign following the El Niño peak. Thus, the GCA south of the equator and west of the date line relates to a broad region in the central Pacific that is forced by the dominant westerly wind anomaly associated with eastward migration of deep convection. North of the equator, the GCA reflects transitional stages in the local winds that are out of phase with the dominant wind pattern.

To further illustrate the sequence of events in the wind field associated with the modal behavior in the upper ocean, we construct a composite wind stress anomaly during different phases of the El Niño cycle as referenced by EOF mode 1. Here, time zero refers to winds averaged during peaks in EOF mode 1, or the mature phase of El Niño (Fig. 11). The 6-month lead and lag times denote relative maxima and minima in mode 2 amplitude, and periods of increasing and decreasing mode 1 amplitude, respectively. Twelve months prior to the peak of El Niño, weak wind anomalies extend across the basin (Fig. 11a). At 6 months lead, anomalous eastward winds develop in the western North Pacific between 120° and 160°E (Fig. 11b), as previously noted by Wang (1995). These winds contribute to a positive curl anomaly north of the equator, consistent with the local fall in sea level associated with EOF mode 2 and an eastward GCA in the NECC in the western Pacific. In the central Pacific, westerly wind anomalies on the equator and near 20°S favor a sea level convergence or rise south of the equator as seen in the sea level EOF mode 2. At the peak of El Niño, anomalous westerly winds in the central Pacific (Fig. 11c) drive eastward current anomalies over a broad region that are known to strongly influence the eastern Pacific through wave propagation (McPhaden et al. 1998). In the western Pacific, this westerly wind anomaly is more apparent south of the equator than north, consistent with the SEC being more directly affected than the NECC. In fact, north of the equator the wind anomaly tends to be more easterly at this time when the NECC begins to exhibit a transition from eastward to westward anomaly. At 6 months lag, weak wind anomalies again prevail (Fig. 11d). During this time there is a tendency for an anomalous rise in sea level north of the equator and a fall in the south in the regions identified in the mode 2 sea level pattern. Meanwhile the mode 1 variability reverts back to pre-El Niño conditions as the trade winds reestablish.

6. Summary and discussion

We have used sea level gradients derived from tide gauges to compute interannual GCAs from 1975 to 1997 in the western Pacific from 2° to 7°N/S. The validity of these current estimates is tested by comparison with similarly derived GCAs from T/P altimeter data. The tide gauge and T/P estimates are highly correlated both north and south of the equator, suggesting that the network of island tide gauges in the western Pacific can monitor interannual changes in the NECC and SEC.

The GCAs behave differently north and south of the equator during various phases of an ENSO event. In the western Pacific, the NECC anomalies are out of phase with fluctuations in the SEC, leading to a north–south asymmetry in transport.

A similar behavior was reported by [Meyers and Donguy \(1984\)](#) for the 1982–83 El Niño, but to our knowledge, ours is the first long record that demonstrates a persistent asymmetry in the GCAs north and south of the equator in this region. In particular, previous studies suggest a more symmetric zonal current response in the central Pacific ([Wyrтки 1979](#); [Taft and Kessler 1991](#)). This GCA asymmetry is associated with a larger-scale adjustment of the upper ocean as represented by the two dominant sea level EOF modes ([Figs. 4](#) and [5](#)). South of the equator the GCA tends to stay in phase with El Niño, that is, the current correlates with the SOI or EOF mode 1. North of the equator, the current correlates with El Niño transitions or EOF mode 2. An eastward anomaly develops prior to the peak phase of El Niño and a westward anomaly follows the peak. These coincide with falling and rising sea level in the same region. The north–south asymmetry is robust as it is not only seen in the GCAs and sea level but also in HS400 and SST fields, which provide greater spatial coverage than the tide gauge data. During the two La Niña events that occurred during the analysis period, the phase differences observed during El Niños are not apparent, although the amplitude response is greater in the SEC than the NECC.

The GCAs both north and south of the equator are related to local ZWS anomalies ([Fig. 9](#)). Near 10°N in the western Pacific, westerly ZWS and an associated positive wind stress curl occur during the onset of an El Niño, which are upwelling favorable and act to lower sea level ([Fig. 11b](#)). This raises the thermocline and tends to enhance the eastward NECC. At the same time, winds near the date line impact the region south of the equator in the opposite sense; that is, the sea level rises locally. East of the date line the wind anomaly becomes more symmetric across the equator during the mature phase of an El Niño ([Fig. 11c](#)). Following the peak phase of an El Niño as the trades reestablish, the GCA turns westward north of the equator and sea level tends to rise slightly earlier north than south of the equator.

In the central and eastern Pacific, GCAs have been reported to be more symmetric (i.e., in phase) across the equator ([Wyrтки 1979](#); [Taft and Kessler 1991](#)), presumably due to the symmetry of the wind forcing and the generation of symmetric wave behavior. In contrast, our findings indicate that the western Pacific transport anomalies in the NECC and SEC are more typically out of phase. In this region, which is more directly wind-forced than the eastern Pacific, the asymmetry of the current response is consistent with similar patterns in the local wind field.

We have focused on the importance of local wind forcing in determining GCAs in the western Pacific largely due to the correspondence between the wind and current time series. We note, however, that the ocean response to wind forcing involves wave propagation both on and off the equator and we cannot dismiss the importance of wave variability in determining the GCAs in this region. Indeed, the maximum correlation between winds and currents north of the equator occurs at a 2-month lag, suggesting propagation effects. In addition, the EOF modes themselves represent phase propagation during El Niños. Modes 1 and 2 combined can account for eastward phase propagation along the equator and westward propagation north of the equator ([Tourre and White 1995](#); [Zhang and Levitus 1996](#)), arising from Kelvin and Rossby wave modes as well as phase variations in the wind field. That the GCAs so closely correlate with these modes implies a close relationship to wave variability. In particular, the westward propagating Rossby waves that have been observed north of the equator ([Kessler 1990](#)) would impact the GCAs in the NECC region. Because these are fast moving waves within 8° of the equator and because the wind forcing has such long zonal scales in this region ([Fig. 11](#)), we do not make a distinction here between local or remote (i.e., slightly to the east) wind forcing with regard to the GCAs north of the equator. To our knowledge, comparable long Rossby waves are not as pronounced south of the equator, consistent with the equatorial asymmetry of the wind and current patterns presented here.

The migration of westerly wind anomalies to the central Pacific is the dominant wind forcing event during El Niños. It appears that equatorial asymmetries in the wind field during this transition lead to the different current anomalies and sea level response in the western Pacific north and south of the equator. It seems likely that the presence of New Guinea and Australia south of the equator compared to the open ocean north of the equator may contribute to asymmetries in the winds, GCA, or both. Moreover, the SPCZ is known to migrate eastward during El Niño events, which contributes to the asymmetry in winds north and south of the equator. During La Niñas when the SPCZ retreats westward, the wind asymmetry is presumably less pronounced and so too the GCA asymmetry is less obvious than during warm events.

We have treated the two current regions from a purely Eulerian view. It is clear from the XBT surveys ([Meyers and Donguy 1984](#)) that meridional displacements of the SEC and NECC do occur. Thus, the weakening of the SEC between 2°S and 7°S may reflect a southward shift of the SEC, as reported for the 1982–83 El Niño ([Meyers and Donguy 1984](#)), rather than a deceleration of the SEC as a whole. Our results then must be interpreted as local changes in the strength of the NECC and SEC rather than a measure of the total transport within these current systems. A more thorough analysis using altimeter data will provide more insight into these effects.

Whether the GCAs represent Eulerian or Lagrangian variations, we conclude by considering the local transport associated with the off-equatorial GCAs. If we assume that the influence of the surface GCAs in this region can be modeled as a uniform current to 100-m depth, the anomalous transport associated with the zonal geostrophic current has peak amplitudes of approximately 10 Sv ($\text{Sv} \equiv 10^6 \text{ m}^3 \text{ s}^{-1}$) between 2° and 7° north and south of the equator during ENSO events. According to [Meyers and Donguy \(1984\)](#), this volume transport is sufficient to cause significant draining of the warm pool region over a 6-month period (i.e., 10 Sv is required to remove the 110-m-thick layer of 28° and 29°C water from the region 1°S–5°N, 140°–160°E over 6 months). Our results suggest that GCA contributions to this drainage, and subsequent

replenishment, occur at different stages and with different amplitudes north and south of the equator during El Niño events. Preliminary analysis of recent sea level data indicate that the 1997–98 El Niño is consistent with this general pattern.

Acknowledgments

This paper benefited from our discussions with Gary Mitchum, Klaus Wyrтки, and Bin Wang and from comments by two anonymous reviewers. We are grateful to Shikiko Nakahara for programming support. TOPEX/Poseidon monthly sea level anomalies were obtained from the NOAA Laboratory for Satellite Altimetry, Reynolds SST monthly data were obtained from the National Meteorological Center, heat storage monthly data were obtained from the Joint Environmental Data Analysis Center at the Scripps Institution of Oceanography, and wind data were obtained from The Florida State University's Center for Ocean–Atmospheric Prediction Studies. This research was supported by the Office of Global Programs, NOAA Grant NA67RJ0154.

REFERENCES

- Cheney, B., L. Miller, R. Agreen, N. Doyle, and J. Lillibridge, 1994: TOPEX/POSEIDON: The 2-cm solution. *J. Geophys. Res.*, **99**, 24 555–24 564..
- Delcroix, T., and J. Picaut, 1998: Zonal displacements of the western equatorial Pacific fresh pool. *J. Geophys. Res.*, **103**, 1087–1098..
- , J.-P. Boulanger, F. Masia, and C. Menkes, 1994: Geosat-derived sea level and surface current anomalies in the equatorial Pacific during the 1986–1989 El Niño and La Niña. *J. Geophys. Res.*, **99**, 25 093–25 107..
- Frankignoul, C., F. Bonjean, and G. Reverdin, 1996: Interannual variability of surface currents in the tropical Pacific during 1987–1993. *J. Geophys. Res.*, **101**, 3629–3647..
- Goldenberg, S. B., and J. J. O'Brien, 1981: Time and space variability of tropical Pacific wind stress. *Mon. Wea. Rev.*, **109**, 1190–1207.. [Find this article online](#)
- Graham, N. E., and W. B. White, 1991: Comments on “On the Role of Off-equatorial Oceanic Rossby Waves during ENSO”. *J. Phys. Oceanogr.*, **21**, 453–460.. [Find this article online](#)
- Ji, M., A. Leetmaa, and J. Derber, 1995: An ocean analysis system for seasonal to interannual climate studies. *Mon. Wea. Rev.*, **123**, 460–481.. [Find this article online](#)
- Kessler, W. S., 1990: Observations of long Rossby waves in the northern tropical Pacific. *J. Geophys. Res.*, **95**, 5183–5217..
- , 1991: Can reflected extra-equatorial Rossby waves drive ENSO? *J. Phys. Oceanogr.*, **21**, 444–452.. [Find this article online](#)
- , and B. A. Taft, 1987: Dynamic heights and zonal geostrophic transports in the central tropical Pacific during 1979–84. *J. Phys. Oceanogr.*, **17**, 97–122.. [Find this article online](#)
- , and M. J. McPhaden, 1995: The 1991–1993 El Niño in the central Pacific. *Deep-Sea Res.*, **42**, 295–333..
- Kilonsky, B. J., and P. Caldwell, 1991: In the pursuit of high-quality sea level data. *IEEE Oceans Proc.*, **2**, 669–675..
- Latif, M., and M. Flügel, 1991: An investigation of short-range climate predictability in the tropical Pacific. *J. Geophys. Res.*, **96**, 2661–2673..
- McPhaden, M. J., and Coauthors, 1998: The Tropical Ocean–Global Atmosphere observing system: A decade of progress. *J. Geophys. Res.*, **103**, 14 169–14 240..
- Meyers, G., and J.-R. Donguy, 1984: The North Equatorial Countercurrent and heat storage in the western Pacific Ocean during 1982–83. *Nature*, **312**, 258–260..
- Mitchum, G. T., 1993: Principal component analysis: Basic methods and extensions. *Aha Hulioko'a: Statistical Methods in Oceanography*, P. Müller and D. Henderson, Eds., SOEST Publication Services, 185–199..
- Picaut, J., and T. Delcroix, 1995: Equatorial wave sequence associated with warm pool displacements during the 1986–1989 El Niño–La Niña. *J. Geophys. Res.*, **100**, 18 393–18 408..
- Rébert, J.-P., J. R. Donguy, G. Eldin, and K. Wyrтки, 1985: Relations between sea level, thermocline depth, heat content, and dynamic

height in the tropical Pacific Ocean. *J. Geophys. Res.*, **90**, 11 719–11 725..

Reynolds, R. W., and D. C. Marisco, 1993: An improved real-time global sea surface temperature analysis. *J. Climate*, **6**, 114–119.. [Find this article online](#)

Smith, W. H. F., and P. Wessel, 1990: Gridding with continuous curvature splines in tension. *Geophysics*, **55**, 293–305..

Taft, B. A., and W. S. Kessler, 1991: Variations of zonal currents in the central tropical Pacific during 1970 to 1987: Sea level and dynamic height measurements. *J. Geophys. Res.*, **96**, 12 599–12 618..

Tourre, Y. M., and W. B. White, 1995: ENSO signals in global upper-ocean temperature. *J. Phys. Oceanogr.*, **25**, 1317–1332.. [Find this article online](#)

Wang, B., 1995: Interdecadal changes in El Niño onset in the last four decades. *J. Climate*, **8**, 267–285.. [Find this article online](#)

Wessel, P., and W. H. F. Smith, 1995: New version of the generic mapping tools released. *Eos, Trans. Amer. Geophys. Union*, **76**, 329..

White, W. B., 1994: Slow El Niño–Southern Oscillation boundary waves. *J. Geophys. Res.*, **99**, 22 737–22 751..

Wyrtki, K., 1974a: Equatorial currents in the Pacific 1950 to 1970 and their relations to the trade winds. *J. Phys. Oceanogr.*, **4**, 372–380.. [Find this article online](#)

— , 1974b: Sea level and the seasonal fluctuations of the equatorial currents in the western Pacific Ocean. *J. Phys. Oceanogr.*, **4**, 91–103.. [Find this article online](#)

— , 1977: Sea level during the 1972 El Niño. *J. Phys. Oceanogr.*, **7**, 779–787.. [Find this article online](#)

— , 1979: The response of sea surface topography to the 1976 El Niño. *J. Phys. Oceanogr.*, **9**, 1223–1231.. [Find this article online](#)

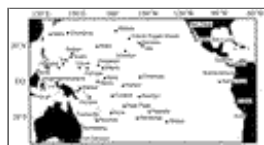
— , 1985: Water displacements in the Pacific and genesis of El Niño cycles. *J. Geophys. Res.*, **90**, 7129–7132..

— , and J. Wenzel, 1984: Possible gyre–gyre interaction in the Pacific Ocean. *Nature*, **309**, 538–540..

Zhang, R.-H., and S. Levitus, 1996: Structure and evolution of interannual variability of the tropical Pacific upper ocean temperature. *J. Geophys. Res.*, **101**, 20 501–20 524..

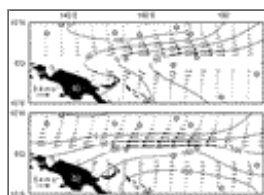
— , and — , 1997: Interannual variability of the coupled tropical Pacific Ocean–atmosphere system associated with the El Niño–Southern Oscillation. *J. Climate*, **10**, 1312–1330.. [Find this article online](#)

Figures



[Click on thumbnail for full-sized image.](#)

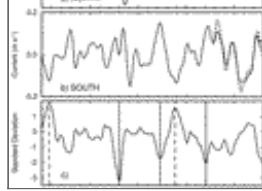
Fig. 1. Tide gauges with records extending over most of the time period from 1975 to 1998.



[Click on thumbnail for full-sized image.](#)

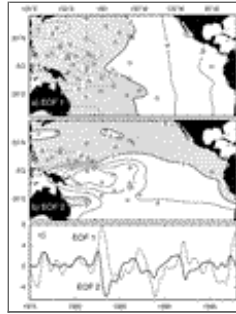
Fig. 2. GCAs derived from sea level anomalies for (a) July 1982 and (b) July 1983. The scale vector indicates an eastward current of 0.4 m s^{-1} . Sea level anomalies are contoured at intervals of 50 mm.





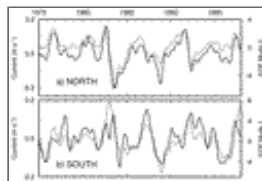
[Click on thumbnail for full-sized image.](#)

Fig. 3. Comparison of time series for tide gauge (solid line) and T/P-derived (dashed line) GCAs: (a) north of the equator averaged over 2°–7°N, 160°E–180° and (b) south of the equator averaged over 2°–7°S, 160°E–180°. (c) The Southern Oscillation index is the normalized difference in sea level pressure between Tahiti and Darwin. The peaks of major El Niño (La Niña) events are indicated by vertical solid (dashed) lines. 1997–98 is also an El Niño year.



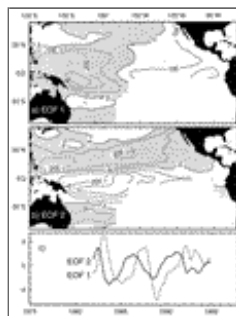
[Click on thumbnail for full-sized image.](#)

Fig. 4. EOF of sea level anomalies (in units of mm): (a) EOF mode 1 explains 42% of the observed variability, while (b) EOF mode 2 accounts for 19%. Tide gauges are indicated by circles. Shading and dashed contours indicate negative anomalies. (c) Temporal expansions for EOF mode 1 (dashed line) and EOF mode 2 (solid line).



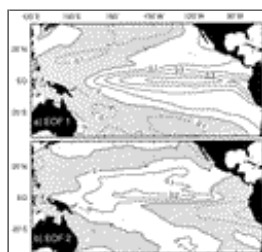
[Click on thumbnail for full-sized image.](#)

Fig. 5. Time series for tide gauge GCAs (solid line) in the region (a) north of the equator averaged over 2°–7°N, 140°–160°E and (b) south of the equator averaged over 2°–7°S, 160°E–180° compared to temporal expansions for (a) sea level EOF mode 2 and (b) EOF mode 1.



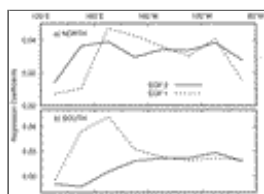
[Click on thumbnail for full-sized image.](#)

Fig. 6. HS400 component (in units of MJ m^{-2}) of combined EOF analysis of HS400, SST, and sea level anomalies. (a) HS400 EOF mode 1 explains 37% of the observed variability, while (b) HS400 EOF mode 2 accounts for 20%. Shading and dashed contours indicate negative anomalies. (c) Temporal expansions for EOF mode 1 (dashed line) and EOF mode 2 (solid line).



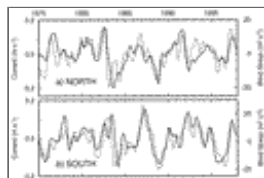
[Click on thumbnail for full-sized image.](#)

Fig. 7. SST component (in units of °C) of combined EOF analysis of HS400, SST, and sea level anomalies. (a) SST EOF mode 1 captures 54% of the observed variability, while EOF mode 2 accounts for 9%. Temporal expansions are given in [Fig. 6c](#). Shading and dashed contours indicate negative anomalies.



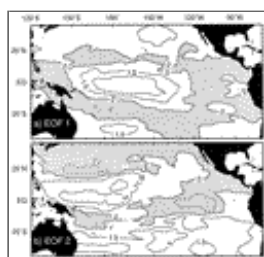
[Click on thumbnail for full-sized image.](#)

Fig. 8. Linear regression of sea level EOF mode 1 (dashed line) and EOF mode 2 (solid line) temporal expansions ([Fig. 4c](#)) onto T/P GCAs averaged over 20° boxes (i.e., from 120° to 140°E, 140° to 160°E, etc.) for the region (a) north of the equator from 2° to 7°N and (b) south of the equator from 2° to 7°S.



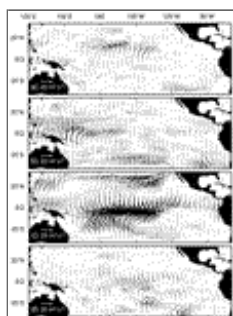
[Click on thumbnail for full-sized image.](#)

Fig. 9. Time series for tide gauge–derived GCAs (solid line) (a) north of the equator averaged over 2°–7°N and 140°–160°E and (b) south of the equator averaged over 2°–7°S and 160°E–180° compared to ZWS anomalies (dashed line) averaged over the same regions.



[Click on thumbnail for full-sized image.](#)

Fig. 10. Linear regression of combined EOF temporal expansions ([Fig. 6c](#)) onto ZWS anomalies (in units of $\text{m}^2 \text{s}^{-2}$) for (a) EOF mode 1 explaining 19% of the variability and (b) EOF mode 2 accounting for 10% of the variability. Shading and dashed contours indicate negative anomalies.



[Click on thumbnail for full-sized image.](#)

Fig. 11. Composite wind stress anomalies for (a) 12-months lead, (b) 6-months lead, (c) 0-months lead, and (d) 6-months lag with respect to El Niño/EOF mode 1 peaks in January 1983, March 1987, and February 1992.



© 2008 American Meteorological Society [Privacy Policy and Disclaimer](#)
Headquarters: 45 Beacon Street Boston, MA 02108-3693
DC Office: 1120 G Street, NW, Suite 800 Washington DC, 20005-3826
amsinfo@ametsoc.org Phone: 617-227-2425 Fax: 617-742-8718
[Allen Press, Inc.](#) assists in the online publication of *AMS* journals.